JOURNAL OF PROPULSION AND POWER
Vol. 20, No. 4, July–August 2004

Interaction of Capillary Plasma with Double-Base and Composite Propellants

Jianquan Li,* Thomas A. Litzinger,† and Stefan T. Thynell†
Pennsylvania State University, University Park, Pennsylvania 16802

Experiments were conducted to characterize the electrothermal capillary plasma and its interaction with a double-base propellant, JA2, and two nitramine composite propellants, M43 and XM39, in closed-chamber and open-air conditions. Pressure–time histories were recorded during ignition and burning of the propellants in the closed chamber. Experimental results indicate significant differences in ignition and combustion of the propellants. The composite propellants exhibited a two-stage burning behavior: one stage of rapid burning driven by the plasma and a second stage of slower self-sustained burning, which occurred with a clear delay after the first stage. During the burning that is driven by the plasma, the burn rate was largely independent of propellant type. Optical microscopic images of recovered propellant samples showed clear physical changes in surface and possibly in subsurface structure, an indication of in-depth melting, vaporization, and possibly chemical reactions. Plasma-induced mass losses for the three propellants were obtained from open-air testing and compared to the values calculated based on the pressure data from closed-chamber tests.

Nomenclature

E = discharge energy (stored energy in the capacitors)
e = electron charge
i_1 = electrical current flowing through the capillary plasma
i_2 = electrical current flowing parallel to the capillary plasma
L_c = capillary length
$L_{\text{n-p}}$ = distance between nozzle exit and stagnation plate
$L_{\text{n-s}}$ = distance between nozzle exit and propellant sample
m_{ab} = ablated mass of test propellant samples
m_e = electron mass
n_e = electron number density
p = pressure
$p_{\max}$ = maximum pressure
R_p = resistance of plasma within capillary
r_c = capillary diameter
t = time
$\nu_{\text{e-n}}$ = collision frequency between electron and neutrals
$\nu_{\text{e-i}}$ = collision frequency between electron and ions
σ = conductivity of plasma within capillary

Introduction

EVOLVED from the electrothermal (ET) propulsion concept, which uses electrical energy and a nonenergetic working fluid, the electrothermal chemical (ETC) technique greatly reduces the requirement for electrical energy by including chemical energy of energetic propellants and, hence, makes possible short-term gun system upgrades. ETC guns introduce electrical energy in the form of ET plasma produced through exploding a metallic wire and sustained by the ablation of surrounding capillary wall material of either the propellant[1] or an inert polymer.[2–6] Because electrical energy can be introduced to the interior ballistic process at desired moments through preprogramming the pulsed power system, the ETC process can be used to ignite the propellant charge, control its burn rate during combustion,[7] and even enhance in-bore acceleration of the projectile in the postcombustion phase.[8] However, recent research on large-caliber ETC guns showed that the benefits gained from combustion control and postcombustion enhancement are outweighed by the amount of electrical energy consumed.[9] Thus, current developments of the ETC process are being focused mainly on the use of ET plasma in the ignition phase.[10]

Results from laboratory experiments and actual firing tests have clearly indicated that ETC plasma ignition can offer several attractive benefits over conventional chemical powder ignition, including precision ignition in terms of shorter and more reproducible ignition delay,[11] mitigation of gun performance sensitivity to ambient temperature,[12,13] and the ability to reliably ignite low-vulnerability ammunition propellants[14] and high-loading-density propellant charges.[15,16] However, optimization of the ETC igniter design relies on a clear and complete understanding of the underlying fundamentals that account for these observed benefits.

Over the years, substantial research activities have been conducted on the subject of plasma–propellant interaction (PPI) and through these research efforts several hypotheses have been proposed to describe the processes during PPI. One of these hypotheses is that radiant heat flux from the plasma to the propellant can lead to in-depth heating of the propellant so that it burns at higher temperatures with an enhanced burn rate[1,17]; another hypothesis is that plasma species can augment the chemical kinetics at or near the propellant surface[17]; a third one is that the mechanical impact is important, because it may produce increased surface area of the propellant through fracture and, hence, increase the burn rate[17]; and recently it was postulated that metallic vapor deposition can be an important heat transfer mechanism in the ignition phase.[18–20] These research efforts have provided many insights into the various mechanisms and, hence, a greatly improved understanding of PPI mechanisms. However, more complete understanding is critical to the development of the ETC technology; therefore, continuing research is needed.

This paper reports results from recent experimental work on characterizing the capillary plasma and its interactions with a double-base propellant, JA2, and two nitramine composite propellants, M43 and XM39, under closed-chamber and open-air conditions. The overall objective of this work is to gain insights from parametric studies that will contribute to the formulation of a complete understanding of the various chemical and physical processes occurring in PPIs.

Received 9 May 2003; revision received 3 January 2004; accepted for publication 19 January 2004.

*Research Assistant, Department of Mechanical and Nuclear Engineering. Member AIAA.

†Professor, Department of Mechanical and Nuclear Engineering. Member AIAA.

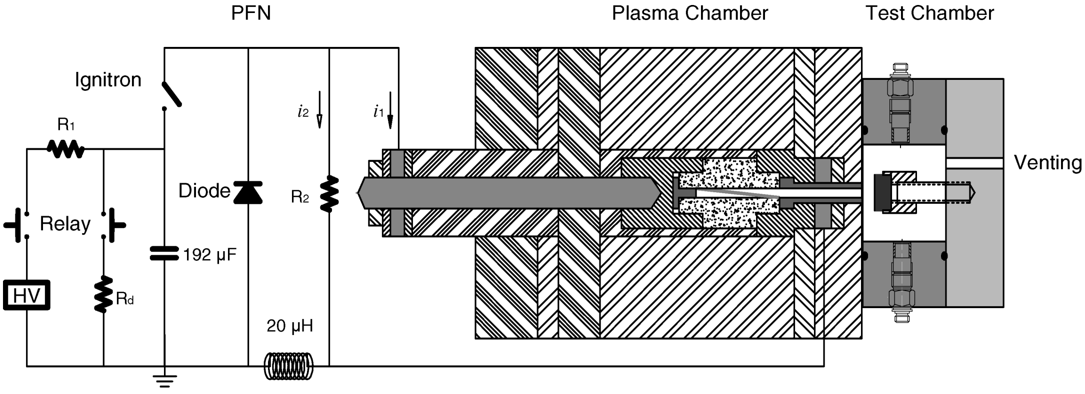

Fig. 1 Schematic of the experimental setup in closed-chamber testing.

Experimental Apparatus and Approach

Plasma Generator

The capillary plasma generation system is schematically shown in Fig. 1. The pulse-forming network (PFN) is based on a resistance–inductance–capacitor circuit, which is mainly composed of an energy storage component that consists of two high-voltage fast-discharge capacitors connected in parallel to yield a total capacitance of 192 μF, pulse-shaping components including a 20-μH inductor and a crowbar diode, and a floating high-voltage mercury switch (ignitron) as the trigger unit. The capacitors can be charged up to 10 kV yielding a maximum energy storage of 9.6 kJ. The plasma chamber consists of a capillary liner, a fine metallic wire, electrodes, and other conducting or nonconducting housing hardware. The capillary liner is typically made of either high-density polyethylene (PE, $[C_2H_4]_n$) or polycarbonate (Lexan, $[C_{16}H_{14}O_3]_n$), which is machined to have a bore length of 26 mm and a typical diameter of 3.2 mm. Located at each end of the capillary are two electrodes made of elkonite, a copper–tungsten alloy (30% Cu, 70% W), which is resistant to material erosion. A fine copper filament of 0.16-mm diam, which runs through the capillary and connects the electrodes, serves as the discharge initiator. After being formed immediately upon triggering the ignitron, the plasma flows through a nozzle that has dimensions of 3.2 mm (orifice diameter) and 26 mm (length) into open air or a closed chamber. The nozzle is designed to have this length simply for accommodating to the dimensions of the plasma chamber.

Test Section

Basically, two test configurations were used in this experimental work; one uses a closed chamber and the other is in open air. Figure 1 shows the closed chamber, which has a typical volume of 6.5 cm^3 that can be varied as needed by using different inserts. A sample holder, with one end screwed into the endplate of the closed chamber, brings the propellant samples close to the nozzle exit to enable normal exposure to the plasma jet. Two pressure transducers are mounted in different locations to allow simultaneous measurement of pressure–time history in the chamber. A venting hole is connected to a solenoid valve for depressurization of the chamber after a test. The instrumented plates in the open-air testing (not shown in Fig. 1) were equipped with either pressure transducers for stagnation pressure measurements or a sample holder for the propellant samples.

Diagnostics

Diagnostic measurements for this work include open-air stagnation pressure of the plasma jet, chamber pressures resulting from plasma expansion and propellant combustion, electrical current i_1 flowing through the capillary plasma and the current i_2 though a noninductive resistor bank (denoted as R_2 in Fig. 1), propellant ablation mass loss caused by exposure to plasma in open-air normal impingement, plasma emission images, and optical microscopy of the surface structure of propellant samples after exposure to the plasma.

Two types of Kistler pressure transducers were used: model 211B3 had a measuring range of 0–500 psig and a rise time of 2 μs for open-air stagnation pressure measurement, and model 211B1 had a much higher measuring range of 0–10,000 psig and a rise time of 1 μs for the chamber pressure measurements. To minimize thermal and electromagnetic effects of plasma on the pressure transducers in closed-chamber testing, recess mounting was used to allow the sensing area of the pressure transducer to be covered by a thin layer ($\sim$1 mm) of vacuum grease, whereas open-air testing used flush mounting of the pressure transducers, which were covered by one strip of electrical insulation tape. These treatments proved to be very effective in protecting the pressure transducers from overheating and from direct exposure to the charged particles in the plasma. A check with compressed air showed no evidence that the grease layer or the tape affected the rise time of the pressure transducer.

Pearson coils were used to measure the instantaneous currents of i_1 and i_2. The instantaneous voltage across the plasma can then be deduced from i_2 and the resistance of R_2, which is connected in parallel with the flow of i_1.

The ablation mass losses of propellants were obtained by weighing the sample before and after a test using a microscale and, to determine consistency, an averaged value from at least two tests under the same conditions was used.

Plasma jet emission images were taken using an intensified, multiple charge-coupled device (CCD) imaging system, Cordin 222-B, which consists of eight CCDs and is capable of acquiring 16 images, each with a pixel resolution of 1,300 by 1,030, a 10-bit dynamic range, and exposure gates down to 10 ns. The first eight images can be acquired at a framing speed of up to 10^8 frames per second, followed by a delay of approximately 1 μs, and then a second set of 8 images at the same framing rate is acquired.

Optical microscopy of plasma-exposed propellant samples was performed with an Olympus FluoView 300 confocal laser scanning microscope (LSM). Both fluorescence images (reflected light) and differential interference contrast (DIC) images (transmitted light) were taken for a morphological analysis of recovered propellant samples. A Nicolet 120 MultiPro data acquisition system along with its ProView software was used for pressure and current measurements.

Results and Discussion

Electrical Parameters Measurements

Figure 2 shows a typical result of the electrical parameters of capillary discharge. The power, energy, and resistance traces were deduced from the measured current and voltage across the capillary. The general trends in these parameters are quite similar for all tests under a given condition. Discharge of the capacitor begins upon triggering the ignitron switch, and ohmic heating of the wire quickly increases the voltage across it and initiates a process of melting, fragmenting, and vaporizing of the wire. The spikes appearing on resistance traces at early times represent the exploding process of the thin wire. The sharp peaks on the voltage trace (known as "wire burst"[18]), corresponding to the last spike on the resistance curve at 11 μs, indicate the completion of the wire explosion and the formation of an initial plasma, which enables electrical conductance

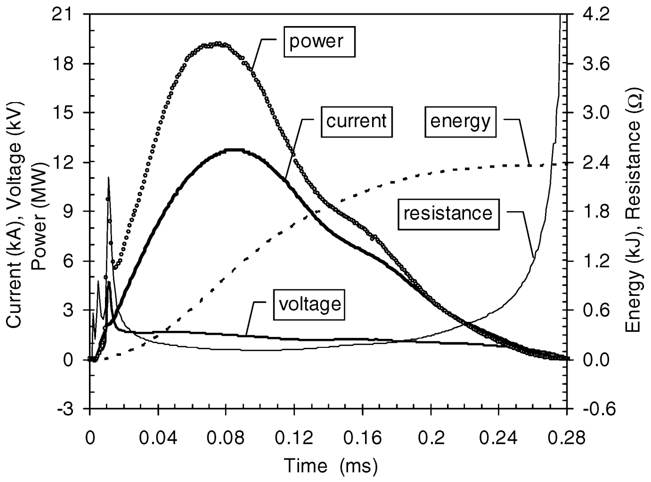

Fig. 2 Electrical parameters of the capillary plasma (3.2-mm capillary bore, $E = 2.40$ kJ).

of the circuit to continue. A small change of slope in the current profile occurs at this time due to the shift of conducting medium from the metallic wire to charged particles in the plasma.

As more energy input proceeds, ohmic heating increases the temperature of the initial plasma to a sufficiently high level to cause ablation of the capillary wall material (including the end electrode) due to the extremely high flux of radiative energy.[21] Vaporization and ionization of the ablated material then produce much more plasma, causing a sharp reduction in resistance. After this sharp decrease, the resistance continues to decrease more slowly and then eventually increases. The variation of resistance is an indication of change in electron number density and in the collision frequencies between electrons and other particles. This dependence is expressed in the equation for plasma resistance R_p (Ref. 22):

$$R_p = L_c \big/ \sigma \pi r_c^2 \tag{1}$$

where L_c and r_c are the capillary length and diameter, respectively, and σ is the plasma conductivity, given by

$$\sigma = \frac{n_e e^2}{m_e(\nu_{\text{e-n}} + \nu_{\text{e-i}})} \tag{2}$$

where n_e, e, and m_e are the electron number density, charge, and mass, respectively; $\nu_{\text{e-n}}$ and $\nu_{\text{e-i}}$ are the collision frequencies of electron neutrals and electron ions. Clearly, the amount of plasma in the capillary strongly affects the resistance through n_e and $\nu_{\text{e-n}}$ plus $\nu_{\text{e-i}}$. Within the capillary, the amount of plasma is determined by two simultaneously occurring processes: addition from ablation of capillary material and reduction due to flow out of the capillary. These two effects will reach a dynamic balance, which does not necessarily occur at the minimum R_p.

During the plasma discharge, the voltage across the capillary changes very little. Consequently, variation of the current is determined by the variation in the resistance. The current reaches a peak value of 12.7 kA at ~85 μs, after which it starts to decrease until the completion of discharge at ~280 μs, where the current drops to zero and the resistance rises up to infinity. Most of the energy initially stored in the capacitor (2.40 kJ) is deposited into the plasma (2.36 kJ) and only a small portion (~1.6%) is consumed in resistive losses and/or remains in the capacitor as residue. The power curve indicates that the electrical energy from the capacitor is discharged to the capillary plasma at varying rates, which reach a maximum of 19.2 MW at 77 μs, slightly earlier than the appearance of the peak current.

Gasdynamic Behaviors of Capillary Plasma

Figure 3 shows two plasma images captured by the CCD camera as well as the experimental configurations for these tests. In Fig. 3a, the plasma fires into open air and impinges on a stagnation plate on which a pressure transducer was mounted, and the nozzle-to-plate distance, $L_{\text{n-p}}$, is 40 mm. In Fig. 3b, the propellant sample is located on a sample holder with a nozzle-to-sample distance, $L_{\text{n-s}}$, of 5 mm. The two tests used the same charging voltage at 4 kV and polyethylene capillaries with a bore of 3.2 mm. Both images were taken with the same exposure time and aperture.

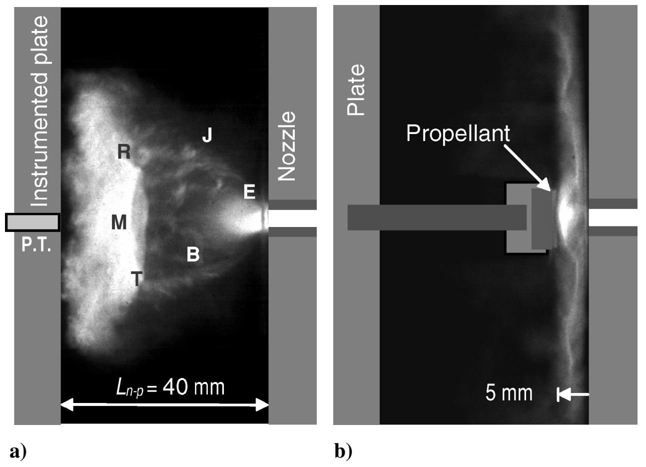

a) b)

Fig. 3 Dynamic structures of plasma jets in open air showing the following features: a) underexpanded supersonic jet and b) "swan-shaped" shock system.

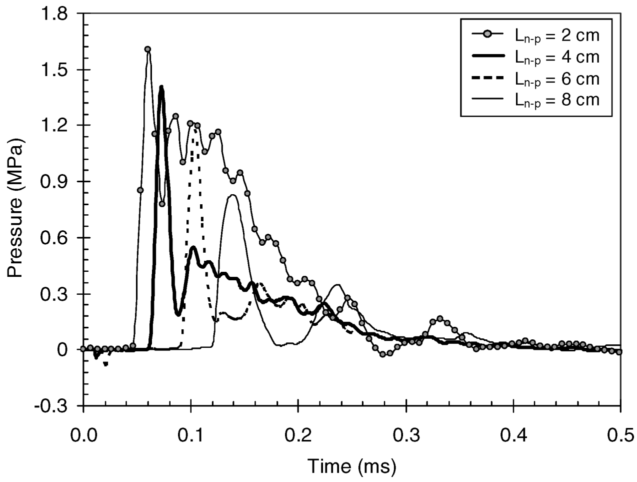

Fig. 4 Stagnation pressures at different nozzle-to-plate distances ($E = 1.56$ kJ).

The image shown in Fig. 3a was taken at $t = 90$ μs after the initiation of discharge. This plasma image exhibits gasdynamic features that are typical of highly underexpanded supersonic jets.[23-25] Several letter labels are used in the picture to indicate key features of the jet. Expansion waves (Prandtl–Meyer fan, labeled E) that are formed at the nozzle exit expand into the ambient open air and extend to the jet boundary (J). They are reflected from there as weak compression waves, which then coalesce to form a strong oblique shock or barrel shock (B) within the plasma jet boundary. Due to the high source pressure inside the capillary, the barrel shock undergoes an irregular reflection, or Mach reflection, to form a triple point (T) at the conjunction of the barrel shock, a reflected shock (R), and a slightly curved strong normal shock or Mach disk (M). As the jet impinges on the perpendicular plate, it is decelerated and redirected, producing a flow in the radial direction along the plate.[26] The presence of the plate makes the plasma jet flow even more complex than that of the freely expanding plasma jets.[27-29] As a result of interaction with the plate, the surface pressure on the plate oscillates, as can be seen in the pressure data presented in Fig. 4. The plasma image also shows what appear to be many small eddies surrounding the barrel shock. These eddies are believed to be caused by plasma mixing with air along the shear layer and may also involve chemical reaction of fuel-rich plasma species with air.

The image in Fig. 3b was taken at $t = 105\ \mu s$ with a JA2 sample placed at $L_{n\text{-}s} = 5$ mm. For illustration purposes, the sample and its holder are also shown in the picture. The distinct multiple-shock system that is present in Fig. 3a is replaced by a "Swan-shaped" shock wave developing in the narrow space between the nozzle exit plane and the sample surface plane. This shock structure acts as if a physical plate much larger than the sample existed and confined the plasma within a 5-mm-thick region. No indication of ignition was observed in this test even though the hottest core (dome-shaped) of the plasma was in contact with the propellant for the entire discharge duration ($\sim 270\ \mu s$).

Figure 4 shows stagnation pressure results for tests that were conducted with different nozzle-to-plate distances ($L_{n\text{-}p}$) with 4 kV charging voltage using 3.2-mm bore PE capillaries. Figure 3a shows the typical setup for these tests, where a pressure transducer was mounted in the stagnation plate along the axis of the plasma jet. These tests illustrate the effect of $L_{n\text{-}p}$ on the surface pressure that a propellant sample would experience in normal impingement situations. Information on peak pressure, plasma transit time, and oscillatory variation of pressure is captured in the pressure traces.

The periodic oscillations in pressure traces have also been observed in studies on normal impingement jets that issue from cold gas sources and impinge on solid plates.[23–25] In those cases, a reflected shock, or plate shock, is present due to the reflection of the jet shocks from the stagnation plate. The plate shock interacts with the jet shock system making the flowfield even more complex. Alternating compression regions and expansion regions exist between the plate shock and the plate, and stagnation bubbles or vortices may form underneath with nozzle-to-plate separations and nozzle-exit-to-ambient pressure ratios. The plate shock moves back and forth causing pressure to oscillate. It is reasonable to expect that, when subject to such impingements from hot plasma jets ($T > 10{,}000$ K; see Ref. 29), the propellant will undergo mechanical changes caused by the resulting mechanical and thermal loads, and these changes could play an important role in the subsequent ignition and combustion.

Open-Air Normal Impingement Tests

The open-air impingement tests were conducted using the configuration shown in Fig. 3b, where the nozzle-to-plate distance was fixed but the nozzle-to-sample distance was varied by adjusting the threaded sample holder. Three gun propellants were used in these tests: a double-base propellant, JA2, and two nitramine composites, M43 and XM39.[30] JA2 is somewhat translucent, whereas M43 and XM39 are completely opaque. At ambient conditions, JA2 is much more flexible compared to the other two, and M43 is the most brittle among the three. All these propellants are cylindrical sticks having a diameter of 10.9 mm. JA2 has seven perforations, each having a diameter about 0.5 mm. M43 and XM39 are nonperforated.

Thin disks were cut from the sticks for testing. In the microscopy study, all disk samples have a typical thickness around 1.5 mm, and samples of M43 and XM39 were polished prior to plasma exposure because cutting from sticks results in a very rough surface. With a thickness of 1.5 mm, samples were sometimes broken into several pieces upon the impingement of plasma when sample-to-nozzle distances were small; this was especially true for M43 and XM39. As a result, a relatively large spacing ($L_{n\text{-}s} = 25$ mm) was used in tests designed for microscopic observation. To avoid fracture during open-air tests for measuring ablated masses, thicker samples of about 4 mm were used. However, even with this thickness, samples of M43 and XM39 (especially M43) tended to fragment into several pieces at higher discharge energy and/or closer nozzle-to-sample distances. To be sure that all sample pieces were recovered, a relatively large enclosure of aluminum foil was used, and an averaged mass loss from three tests was determined.

In the open-air testing, parametric studies were performed with variations of $L_{n\text{-}s}$ ranging from 3 to 25 mm and of charging voltage from 2 to 6 kV corresponding to energy levels from 0.38 to 3.46 kJ. Regardless of the conditions, ignition did not occur; the failure to achieve ignition was most likely due to the lack of confinement, because ignition threshold has been shown to be a strong function of confinement.[31] However, the open-air configuration provides an easier way to determine propellant mass losses prior to ignition due to ablation by plasma, because it avoids the need to interrupt the test by, for example, reducing the chamber pressure.

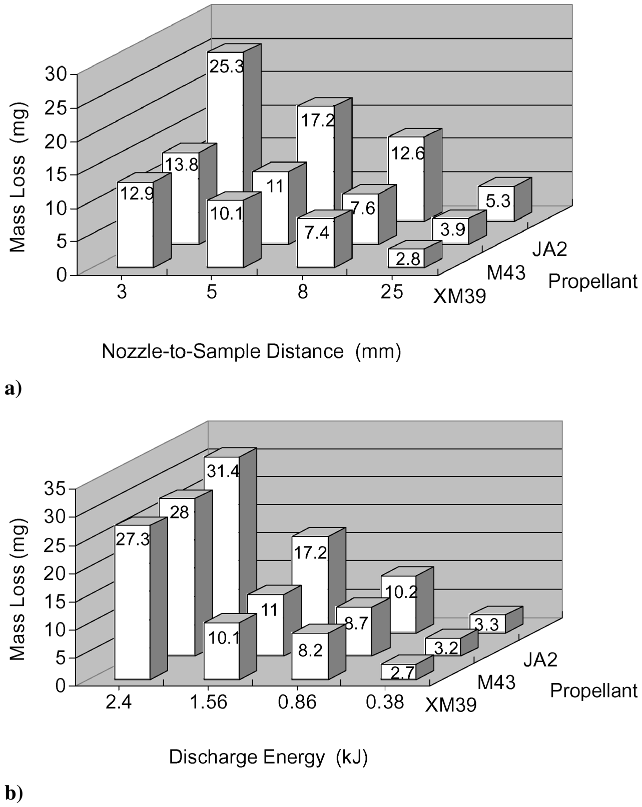

Fig. 5 Ablation masses of the propellants: a) $E = 1.56$ kJ and b) $L_{n\text{-}s} = 5$ mm.

Figure 5a presents typical results for mass losses of the three propellants subject to head-on normal impingement of the capillary plasma at different nozzle-to-sample distances. These tests were conducted using a charging voltage of 4 kV ($E = 1.56$ kJ). Another series of tests was performed at a fixed value of $L_{n\text{-}s}$ but at four different energy levels. These results are presented in Fig. 5b. Table 1 lists the mass losses due to ablation for each individual test, and the information about fragmentation is also included. As can be seen from both sets of results, under the same test conditions, JA2 often has the largest amount of mass loss. Also, the data show the expected trends that higher discharge energy and smaller $L_{n\text{-}s}$ both result in higher mass loss. Another interesting observation is that at higher discharge energy or smaller $L_{n\text{-}s}$ values all three propellants tended to fragment into a few (sometimes many) small pieces (see Table 1 for fragmentation information). This fragmentation would be expected to augment the burn rate.

Two processes can contribute to the mass loss during exposure to the plasma: surface ablation and in-depth eruptive ejection. Surface ablation is caused by intense heating that melts and vaporizes the surface material. During the ablation process, a thin layer of vapor will develop between the plasma and the propellant surface to form a vapor shield,[32–34] which causes a reduction in the radiative energy transport to the propellant surface, suggesting that the plasma kinetic energy may be more important than radiative heat flux.[34] It should be noted that, for the perforated JA2, its seven perforations provide more exposed surface area than the nonperforated composite propellants. However, examination of recovered JA2 samples indicates only a slight enlargement of the perforation (about 0.03–0.05 mm in diameter and 1–1.5 mm in depth), which occurred when higher energy and smaller $L_{n\text{-}s}$ were used; thus, the ablation mass from the perforations accounts for a small portion (about 5%) of the

Table 1 Test-to-test variation in ablation masses of propellants in open-air testing

Test condition		m_{ab_JA2}, mg				m_{ab_M43}, mg				m_{ab_XM39}, mg			
E, kJ	$L_{n\text{-}s}$, mm	Test 1	Test 2	Test 3	Aver.	Test 1	Test 2	Test 3	Aver.	Test 1	Test 2	Test 3	Aver.
0.38	5	3.2	3.3	n/a	**3.3**	3.0	3.3	n/a	**3.2**	2.6	2.8	n/a	**2.7**
0.86	5	9.8	10.5	n/a	**10.2**	8.2	9.1	n/a	**8.7**	7.9	8.5	n/a	**8.2**
1.56	5	16.4	17.2	18.0	**17.2**	9.8[a]	11.4[a]	11.9	**11.0**	9.2	10.1[a]	11.0	**10.1**
2.40	5	29.9[a]	31.5	32.7	**31.4**	27.2[b]	27.8[b]	29.0[b]	**28.0**	26.0[b]	27.4[b]	28.4[b]	**27.3**
1.56	3	24.6	25.3	26.0[a]	**25.3**	12.6[b]	14.0[a]	14.8[a]	**13.8**	12.3[a]	12.9[a]	13.6	**12.9**
1.56	8	12.2	12.6	12.9	**12.6**	7.1	7.7[a]	8.0	**7.6**	7.3	7.4	7.6	**7.4**
1.56	25	5.1	5.4	n/a	**5.3**	3.8	4.0	n/a	**3.9**	2.7	2.8	n/a	**2.8**

[a] Tests with propellant fragmentation (2–5 pieces). [b] Tests with propellant fragmentation (more than 5 pieces).

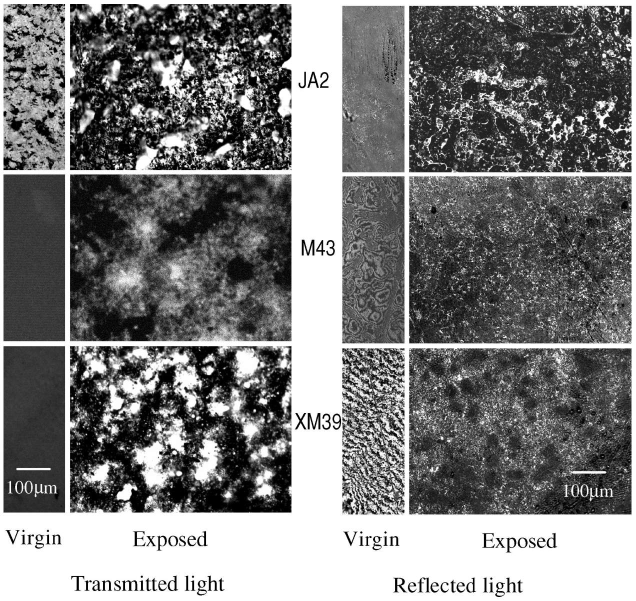

Fig. 6 Microscopic images of plasma-exposed propellant samples ($E = 3.46$ kJ, $L_{n\text{-}s} = 25$ mm).

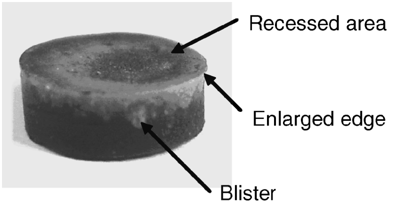

a) Sample thickness: 4.5 mm

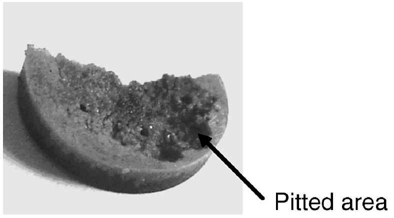

b) Sample thickness: 2 mm

Fig. 7 Photos of recovered JA2 samples ($E = 2.40$ kJ, $L_{n\text{-}s} = 5$ mm).

total amount. Eruptive ejection is a result of the formation of high-pressure gas bubbles in subsurface regions due to in-depth radiative heating, which can occur depending on the optical properties of the propellants.[1,35]

Propellant samples recovered after the tests show significant changes in color and surface structure. Optical microscopic photos of typical results are shown in Fig. 6, where both confocal LSM (reflected light) and DIC (transmitted light) images are presented. Images of virgin samples are included for comparison. Surface modification and/or in-depth structural change were observed for all samples.

Tests of JA2 with higher discharge energies and shorter $L_{n\text{-}s}$ values usually resulted in color change from dark green to yellow-green in a layer from the exposed surface down to about 1 to 1.5 mm of the sample, and internal voids and blisters were observed along the side surface of this layer. A very roughly pitted area about 6 mm in diameter that was recessed about 0.5–1.0 mm from the original surface was found in the region that was directly exposed to the plasma. Also, deformation of the affected layer causes slight enlargement of the diameter. Figure 7 shows two JA2 samples recovered after being exposed to plasma (5 kV charging voltage with $L_{n\text{-}s} = 5$ mm); one of the samples fragmented due to its small thickness (Fig. 7b).

These observations are a strong indicator that in-depth heating causes decomposition of the propellant. Some of the gaseous decomposition products accumulated in bubbles that burst, leaving pits in the surface; others remained trapped inside the propellant, resulting in internal bubbles and/or blisters. Chemical analysis of NO levels in recovered JA2 samples by Beyer and Pesce-Rodriguez.[36] and Pesce-Rodriguez et al.[37] using desorption gas chromatographymass spectroscopy indicated enhancement of NO formation down to a depth of 0.75 mm from the surface and suggested that NO is an early product of decomposition of nitrate esters and is sufficiently stable to remain trapped inside the sample. The color of the strongly affected region looks black as a result of some residual deposits from the plasma; Taylor[19] suggested that the black region results from deposition of copper oxide (CuO). Slight enlargement in the perforations ranging from 0.03 to 0.05 mm was observed on the exposed side of the JA2 sample, and the affected depth is about 1–1.5 mm, corresponding to a mass loss of about 1–2 mg.

The responses of M43 and XM39 were similar to each other but quite different from that of JA2. The surfaces of M43 and XM39 were blackened, but otherwise no color change was observed. Pits were found in the affected surface areas for these materials, but no blisters or recessed areas were formed. These results suggest that radiative and conductive heating is restricted to a very thin layer in the near-surface zone, and mass losses are caused by surface ablation only. The lack of in-depth effects of the plasma is consistent with the fact that these propellants are opaque, whereas JA2 is somewhat translucent;this effect agrees with the findings by Koleczko et al.[1] The differences between the JA2 and the composite propellants are expected to affect their behavior during ignition and combustion, as will be seen in the closed-chamber results presented in next section.

Ignition and Combustion in Closed Chamber

Closed-chamber testing was conducted in the configuration shown in Fig. 1 to study the plasma ignition and combustion behavior of the three propellants. For each test, approximately 500 mg of propellant was used, corresponding to a loading density of about 0.08 g/cm^3. The plasma impinged normally to the sample surface at a nozzle-to-sample distance of 5 mm, which is a very aggressive condition for mass loss, ignition, and burn rate enhancement.[38] The capacitors were charged to 5 kV ($E = 2.40$ kJ) with about 2.36 kJ energy deposited into the plasma.

Table 2 Summary of plasma ignition and combustion of propellants ($E = 2.40$ kJ)

Propellant type	$\tau_{\text{peak-power}}$, ms	$\tau_{\text{peak-pressure}}$, ms	$\tau_{\text{end-of-pulse}}$, ms	$\tau_{\text{second-stage}}$, ms	$\tau_{\text{end-of-combustion}}$, ms	$\Delta\tau$,[a] ms
JA2	0.081	0.230	0.310	0.31	1.38	1.07
M43	0.078	0.240	0.300	3.24	42.25	39.01
XM39	0.078	0.245	0.310	3.70	62.50	58.80

[a] $\Delta\tau = \tau_{\text{end-of-combustion}} - \tau_{\text{second-stage}}$.

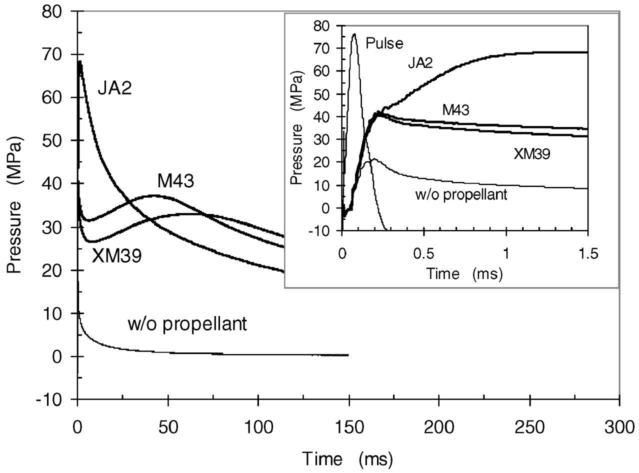

Fig. 8 Comparison of ignition and burning for JA2, M43, and XM39 ($E = 2.40$ kJ).

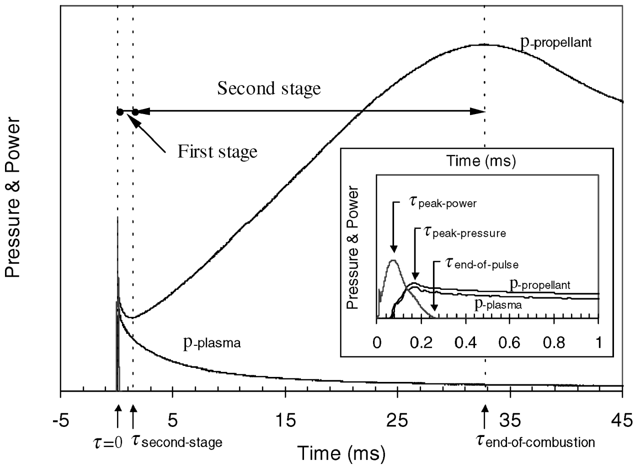

Fig. 9 Illustration of two-stage burning behavior of ETC plasma-ignited propellants.

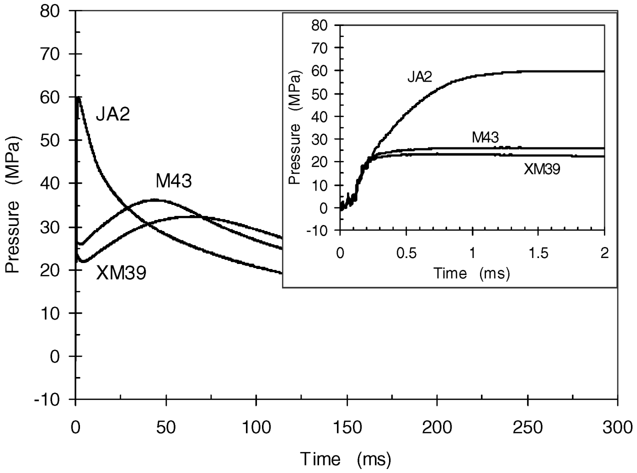

Fig. 10 Comparison of pressure increase as a result of combustion of the propellants.

Pressure histories were recorded for these tests as well as the baseline case with no propellant. Typical results are plotted in Fig. 8 on two time scales, 0 to 300 ms and 0 to 1.5 ms. The shorter timescale plot includes the plasma power to indicate the duration of the plasma pulse. The results show significant differences in both ignition delay and overall burn rate of JA2 and the composite propellants, XM39 and M43. The pressure traces of the composite propellants indicate a two-stage burning behavior, which is most clearly visible for the composite propellants in Fig. 8. During the first stage, which occurs within the plasma pulse, chamber pressure rises rapidly above the pressure caused by the plasma alone (curve labeled "w/o propellant" in Fig. 8.) The increased pressure is caused by the ablation and/or combustion of the propellant. This rapid rise is followed by a decrease in pressure, indicating that the propellant has not ignited. After a delay, the pressure begins to rise again, indicating that the propellant has ignited due to exposure to the high-temperature gases in the chamber; during the second stage, the propellant burns to completion.

Table 2 presents several moments of interest during ignition and combustion. The times presented correspond to peak power ($\tau_{\text{peak-power}}$), first peak pressure ($\tau_{\text{peak-pressure}}$), end of pulse ($\tau_{\text{end-of-pulse}}$), start of the second stage ($\tau_{\text{second-stage}}$), and completion of combustion ($\tau_{\text{end-of-combustion}}$). These particular times are also illustrated in Fig. 9. The moments that are characteristic of plasma-driven ignition and combustion are quite similar for the three propellants. In fact, within the duration of the plasma pulse, the responses of all three propellants, including the pressure rise, are surprisingly similar. A clear delay period after the plasma-driven burning is present only for the composite propellants. Burning in the second stage is much slower as indicated by the large values of $\Delta\tau$ listed in Table 2. XM39 exhibits a longer second stage than M43.

During the first stage, the pressure rise is a combined result of the plasma expansion and ignition/burning of part of the propellant, which includes the ablated mass and part of the main charge. This portion of the propellant is ignited and burned to final products at a very high burn rate as a result of the plasma enhancement. The plasma-enhanced burning within the pulse (the first stage) appears to be quite similar among the propellants.

To estimate the amount of propellant mass that is consumed in the first stage in the closed-chamber tests, an energy balance was performed based on the increase in chamber pressure caused by the burning of the propellant. Subtracting the pressure without propellant from the pressure with propellant yields the pressure data required for the analysis; the pressure difference curves resulting from this subtraction are plotted in Fig. 10. For energy balance, the chamber volume is the control volume and the combustion products are modeled as a mass generation source. Applying the first law of thermodynamics to the control volume and neglecting heat transfer to the walls give an apparent mass generation rate that is related to the pressure variation; that is,

$$\dot{m} = \frac{c_v V}{c_p R T_g / MW} \frac{\mathrm{d}p}{\mathrm{d}t} \tag{3}$$

where V is the chamber volume and T_g and MW are the average temperature and the molecular weight the combustion products, respectively. The gasified mass at any time of interest can be calculated by integration of Eq. (3). Neglecting the heat loss to chamber walls is not expected to introduce a large error given the short time over which the calculation is performed. Also, the subtraction scheme

Table 3 Calculated gasified masses within the plasma pulse ($E = 2.40$ kJ)

Propellant type	$m_{\text{peak-power}}$, mg	$m_{\text{peak-pressure}}$, mg	$m_{\text{end-of-pulse}}$, mg	m_{measured}, mg
JA2	18	147	197	32
M43	17	248	290	28
XM39	18	258	287	27

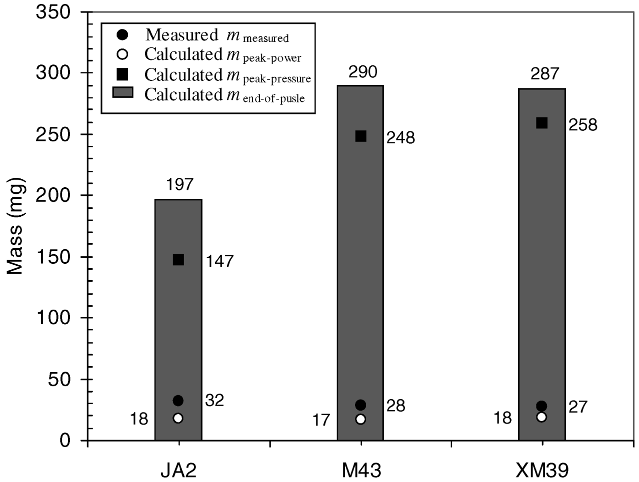

Fig. 11 Comparison of mass losses for JA2, M43, and XM39 ($E = 2.40$ kJ).

will further minimize this error because it reduces the effect of heat loss from the plasma gases.

The total propellant mass calculated through the energy balance is less than the mass of propellant used in the tests. Consequently, the gasification rate is scaled so that the total mass from the calculation matches the propellant mass used. Table 3 summarizes the calculated gasified masses at several particular time intervals that are listed in Table 2; namely, $m_{\text{peak-power}}$, $m_{\text{peak-pressure}}$, and $m_{\text{end-of-pulse}}$ correspond to $\tau_{\text{peak-power}}$, $\tau_{\text{peak-pressure}}$, and $\tau_{\text{end-of-pulse}}$, respectively. For comparison, the measured plasma-induced mass losses (m_{measured}) from open-air experiments are included as well. These results are also presented in Fig. 11.

Based on the calculation, the total mass conversion from solid to gas within the plasma pulse ($m_{\text{end-of-pulse}}$) is much greater than the mass loss measured in open-air testing, m_{measured}. It is not unreasonable for the closed-chamber tests to give higher values because higher gas densities will occur within the subsonic regions of the plasma jet near the sample surface, and the higher densities should enhance the heat transfer to the sample, resulting in increased mass conversion rates from solid to gaseous products. Moreover, it is likely that $m_{\text{end-of-pulse}}$ involves not only the mass loss due to ablation but also due to combustion of propellant that occurs during the first stage; the latter represents a major fraction of $m_{\text{end-of-pulse}}$. It should be noted that the value of $m_{\text{end-of-pulse}}$ for JA2 is smaller than that for the two composites, which is opposite of the trend for the open-air mass loss, m_{measured}, in which JA2 has a larger value than the composites. This opposite trend suggests that, in the closed-chamber testing, the composites have more mass burned during the plasma pulse. During open-air testing the composite propellants fragmented into more pieces than JA2, which often did not fragment at all. Thus, fragmentation of the composite samples may account for their faster combustion during the plasma pulse.

The calculated gas generation rates for the three propellants are presented in Fig. 12, which also includes the combustion pressure curves and the plasma power to indicate the pulse width. The energy balance requires the time derivative of the pressure, which is affected by noise that causes significant scatter in the gas generation rates. To minimize this effect, a 500-Hz low-pass filter was used to remove high-frequency components in the original data. Multiple peaks in gasification rates are present for all propellants, which may correspond to gasification of the ablated mass, combustion of the ablated mass, and combustion of part of the propellant. The gas generation rate curves during the plasma pulse look similar for the three propellants, but JA2 has a lower peak value.

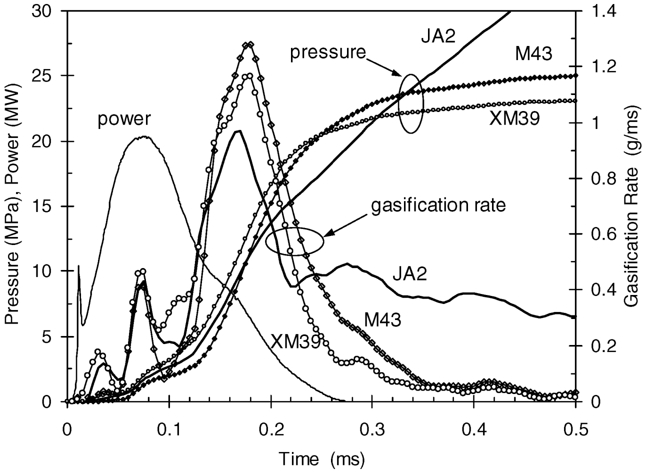

Fig. 12 Comparison of gas generation rates in early stage of burning ($E = 2.40$ kJ).

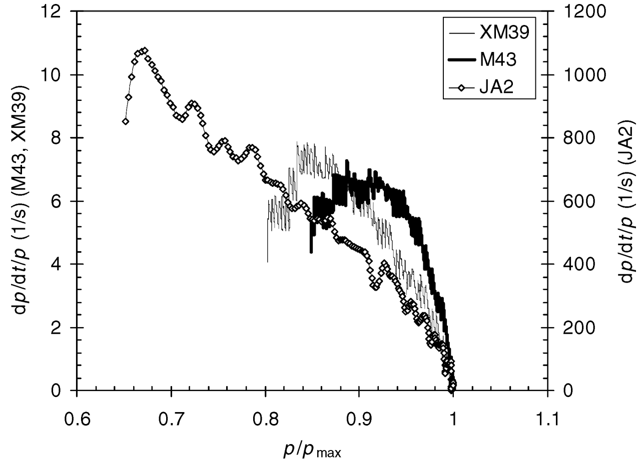

Fig. 13 Comparison of vivacities in the second stage of burning ($E = 2.40$ kJ).

After the plasma pulse, however, the pressure data indicated that the three propellants behave in a significantly different manner. To determine the possible cause of this difference, the dynamic vivacities of the propellants were calculated over the second stage, and the results are shown in Fig. 13. The dynamic vivacity is defined as[39]

$$\text{Vivacity} = \frac{1}{p_{\max}} \cdot \frac{\mathrm{d}}{\mathrm{d}t}(\ell n\, p) = \frac{1}{p_{\max} \cdot p} \cdot \frac{\mathrm{d}p}{\mathrm{d}t} \tag{3}$$

where p is the measured chamber pressure and $p_{\max}$ is its maximum, more popularly defined as the instantaneous time derivative of the experimental pressure divided by that pressure.[2] The plot of the vivacity vs the instantaneous pressure (or scaled by $p_{\max}$) produces very useful information on the burning behavior of the propellant. A steeper curve of vivacity indicates a higher burn rate. Vivacity also indicates whether burning is progressive, a positive slope, or regressive, a negative slope.[2] The results presented in Fig. 13 suggest that all the propellants burn in a similar manner, which is first progressive and then regressive in the second stage of burning, and JA2 burns much faster than the composite propellants M43 and XM39. The faster burning rate of JA2 is due to the higher pressures that exist when it burns compared to the composite propellants, as indicated in Fig. 8.

Conclusions

The characteristics of ET capillary plasma and its interactions with a double-base propellant, JA2, and two nitramine composite propellants, M43 and XM39, were investigated in open-air and closed-chamber configurations. Experimental results include electrical parameters of the plasma pulse, gasdynamic features of plasma jets, plasma-induced mass losses of the propellants, and propellant ignition/burning behaviors in the closed chamber.

Open-air testing results show that the plasma jet exhibits gasdynamic features commonly seen in underexpanded supersonic jets involving a complex shock system. When impinging on a stagnation plate or propellant sample, another shock system, the plate shock, may form as a result of reflection of the jet shock system. Interaction of these shocks may account for the oscillations in the stagnation pressure. High-magnification images of propellant samples after exposure to the plasma in open-air testing indicate modification of surface morphology, which suggests subsurface decomposition of propellant ingredients due to in-depth radiative heating in the JA2 case.

In closed-chamber testing, the composite propellants exhibit a clear two-stage burning behavior, whereas this feature is much less distinct in the case of JA2 propellant because it is easier to ignite than the composites, which were formulated to be low-vulnerability propellants. The results showed significant difference in the gas generation rates during and after the plasma pulse, with a very fast rate within the pulse and much lower rate beyond the pulse; also gas generation rates are largely independent of the propellant type only during the plasma pulse. Plasma-induced mass losses of the propellants cause a fast pressure rise in the first stage of burning. Vivacity results suggest that regressive burning occurs for the three propellants under the test conditions in this work.

Acknowledgments

This work was supported by Army Research Office under contract DAAG55-98-1-0519 with the management of D. M. Mann. The authors are also grateful to Johnny Yu at the ATK-Radford Army Ammunition Plant for the shipment of the JA2 propellant.

References

[1] Koleczko, A., Ehrhardt, W., Kelzenberg, S., and Eisenreich, N., “Plasma Ignition and Combustion,” *Propellants, Explosives, Pyrotechnics*, Vol. 26, No. 2, 2001, pp. 75–83.

[2] Birk, A., Del Guercio, M., Kinkennon, A., Kooker, D. E., and Kaste, P., “Interrupted-Burning Tests of Plasma-Ignited JA2 and M30 Grains in a Closed Chamber,” *Propellants, Explosives, Pyrotechnics*, Vol. 25, No. 3, 2000, pp. 133–142.

[3] Beyer, R. A., “Small-Scale Experiments in Plasma-Propellant Interactions,” U.S. Army Research Lab., Rept. ARL-TR-2598, Aberdeen Proving Ground, MD, Sept. 2001.

[4] Kohel, J. M., Su, L. K., Clemens, N. T., and Varghese, P. L., “Emission Spectroscopic Measurements and Analysis of a Pulsed Plasma Jet,” *IEEE Transactions on Magnetics*, Vol. 35, No. 1, 1999, pp. 201–206.

[5] Li, J. Q., Kwon, J., Thynell, S. T., and Litzinger, T. A., “Experimental Investigations of Characteristics of Electro-Thermal-Chemical Plasma,” AIAA Paper 2001-3855, July 2001.

[6] Edwards, C. M., Bourham, M. A., and Gilligan, J. G., “Experimental Studies of the Plasma-Propellant Interface for Electrothermal-Chemical Launchers,” *IEEE Transactions on Magnetics*, Vol. 35, No. 1, 1999, pp. 404–409.

[7] Katulka, G. L., White, K. J., Oberle, W. F., Kaste, P. J., Pesce-Rodriguez, R. A., and Leadore, M. L., “Experimental Characterization of Plasma Effects on Energetic Materials for Electrothermal-Chemical Launch Applications,” *IEEE Transactions on Magnetics*, Vol. 35, No. 1, 1999, pp. 197–200.

[8] Fuller, S. R., and Woodley, C. R., “Smart Gun for Artillery Muzzle Velocity Control: Simulations and Experimental Proof of Principle,” *IEEE Transactions on Magnetics*, Vol. 37, No. 1, 2001, pp. 157–160.

[9] Taylor, M. J., “Consideration of the Energy Transfer Mechanisms Involved in SPETC Ignition Systems,” *IEEE Transactions on Magnetics*, Vol. 39, No. 1, 2003, pp. 262–268.

[10] Fair, H. D., “Electric Launch Science and Technology in the United States,” *IEEE Transactions on Magnetics*, Vol. 39, No. 1, 2003, pp. 11–17.

[11] Katulka, G. L., and Dyvik, J. A., “Experimental Results of Electrical Plasma Ignition in 120-mm Solid Propellant Tank Gun Firings,” Chemical Propulsion Information Agency Publ. 653, Vol. 3, 1996, pp. 103–110.

[12] Marinos, C., “ETC Ignition and Temperature Sensitivity,” Chemical Propulsion Information Agency Publ. 631, Vol. 3, 1995, pp. 109–118.

[13] Dyvik, J. A., and Katulka, G. L., “ETC Temperature Compensation: Experimental Results of 120-mm Test Firings,” Chemical Propulsion Information Agency Publ. 653, Vol. 1, 1996, pp. 111–119.

[14] Chaboki, A., Zelenak, S., and Isle, B., “Recent Advances in Electrothermal-Chemical Gun Propulsion at United Defense, L. P.,” *IEEE Transactions on Magnetics*, Vol. 33, No. 1, 1997, pp. 284–288.

[15] Wren, G. P., and Oberle, W. F., “Influence of High Loading Density Charge Configurations on Performance of Electrothermal-Chemical (ETC) Guns,” *IEEE Transactions on Magnetics*, Vol. 37, No. 1, 2001, pp. 211–215.

[16] Perelmutter, L., Sudai, M., Goldenberg, C., Kimhe, D., Zeevi, Z., Arie, S., Melnik, M., and Melnik, D., “Plasma Propagation and Ignition in the Chamber of a SPETC Gun,” *IEEE Transactions on Magnetics*, Vol. 35, No. 1, 1999, pp. 213–217.

[17] Wren, G. P., Oberle, W. F., and Hosangadi, A., “Influence of Radiation on Grain Heating in ETC Closed Chambers,” *IEEE Transactions on Magnetics*, Vol. 35, No. 1, 1999, pp. 234–239.

[18] Taylor, M. J., and Dunnett, J., “A Description of the Wire Explosion Process for the ETC Plasma Generators,”*IEEE Transactions on Magnetics*, Vol. 39, No. 1, 2003, pp. 269–274.

[19] Taylor, M. J., “Ignition of Propellant by Metallic Vapour Deposition for an ETC Gun System,” *Propellants, Explosives, Pyrotechnics*, Vol. 26, No. 3, 2001, pp. 137–143.

[20] Taylor, M. J., “Evidence for the Hypothesis of Ignition of Propellants by Metallic Vapour Deposition,” *Propellants, Explosives, Pyrotechnics*, Vol. 27, No. 6, 2002, pp. 327–335.

[21] Ruchti, C. B., and Niemeyer, L., “Ablation Controlled Arcs,” *IEEE Transactions on Plasma Science*, Vol. PS-14, No. 4, 1986, pp. 423–434.

[22] Katulka, G. L., Oberle, W. F., Wren, G. P., Okamitsu, J., and Messina, N. A., “Pulsed-Power and High Energy Plasma Simulations for Application to Electrothermal-Chemical Guns,” *IEEE Transactions on Magnetics*, Vol. 33, No. 1, 1997, pp. 299–304.

[23] Lamont, P. J., and Hunt, B. L., “The Impingement of Underexpanded, Axisymmetric Jets on Perpendicular and Inclined Flat Plates,” *Journal of Fluid Mechanics*, Vol. 100, 1980, pp. 471–511.

[24] Sakakibara, Y., and Iwamoto, J., “Numerical Study of Oscillation Mechanism in Underexpanded Jet Impinging on Plate,” *Journal of Fluids Engineering*, Vol. 120, No. 3, 1998, pp. 477–481.

[25] Crist, S., Sherman, P. M., and Glass, D. R., “Study of the Highly Underexpanded Sonic Jet,” *AIAA Journal*, Vol. 4, No. 1, 1966, pp. 68–71.

[26] Nusca, M. J., McQuaid, M. J., and Anderson, W. R., “Numerical Model of the Plasma Jet Generated by an Electrothermal-Chemical Igniter,” *Journal of Thermophysics and Heat Transfer*, Vol. 16, No. 1, 2002, pp. 157–160.

[27] Kohel, J. M., Su, L. K., Clemens, N. T., and Varghese, P. L., “Emission Spectroscopic Measurements and Analysis of a Pulsed Plasma Jet,” *IEEE Transactions on Magnetics*, Vol. 35, No. 1, 1999, pp. 201–206.

[28] Nusca, M. J., White, K. J., Young, T. R., and Landsberg, A. M., “Computational Simulation and Experimental Visualization of an Open-Air Plasma Discharge,” CPIA Publication 662, Vol. 1, Oct. 1997, pp. 43–56.

[29] Kim, J. U., Clemens, N. T., and Varghese, P. L., “Experimental Study of the Transient Underexpanded Jet Generated by Electrothermal Capillary Plasma,” *Journal of Propulsion and Power*, Vol. 18, No. 6, 2002, pp. 1153–1160.

[30] Fetherolf, B. L., “The Physical and Chemical Processes Governing CO2 Laser-Induced Pyrolysis and Combustion of the Solid Propellants RDX, AND, XM39, and M43,” Ph.D. Dissertation, Dept. of Mechanical Engineering, Pennsylvania State Univ., University Park, PA, 1993.

[31] Huang, T. H., Thynell, S. T., and Kuo, K. K., “Hot Fragment Conductive Ignition of Nitramine-Based Propellants,” *Journal of Propulsion and Power*, Vol. 11, No. 4, 1995, pp. 781–790.

[32] Niemeyer, L., “Evaporation Dominated High Current Arcs in Narrow Channels,” *IEEE Transactions on Power Apparatus and Systems*, Vol. PAS-97, No. 3, 1978, pp. 950–958.

[33] Gilligan, J. G. and Mohanti, R. B., “Time-Dependent Numerical Simulation of Ablation-Controlled Arcs,” *IEEE Transactions on Plasma Science*, Vol. 18, No. 2, 1990, pp. 190–197.

[34] Bourham, M. A., Gilligan, J. G., Hankins, O. E., Mayo, R. M., Nahm, M. L., Sharpe, J. P., and Buchanan, C. D., “Investigation of Geometrical Influence on Plasma-Augmented Burn Rates of JA-2 Solid Propellant for

ETC Guns," Chemical Propulsion Information Agency Publ. 631, Vol. 1, 1995, pp. 103–112.

[35] Kappen, K., and Beyer, R. A., "Progress in Understanding Plasma-Propellant Interaction," *Propellants, Explosives, Pyrotechnics*, Vol. 28, No. 1, 2003, pp. 32–36.

[36] Beyer, R. A., and Pesce-Rodriguez, R. A., "Experiments to Define Plasma-Propellant Interactions," *IEEE Transactions on Magnetics*, Vol. 39, No. 1, 2003, pp. 207–211.

[37] Pesce-Rodriguez, R. A., Beyer, R. A., Kinkennon, A. E., Del Guercio, M., Kaste, P. J., and Newberry, J. E., "In-Depth Chemistry in Plasma-Exposed M30 and JA2 Gun Propellants," U.S. Army Research Lab., Rept. ARL-TR-2505, Aberdeen Proving Ground, MD, June 2001.

[38] Bourham, M. A., Gilligan, J. G., and Oberle, W. F., "Analysis of Solid Propellant Combustion Behavior Under Electrothermal Plasma Injection for ETC Launchers," *IEEE Transactions on Magnetics*, Vol. 33, No. 1, 1997, pp. 278–283.

[39] Engelen, K., and Lefebvre, M. H., "Properties of a Gas-Generating Composition Related to the Particle Size of the Oxidizer," *Propellants, Explosives, Pyrotechnics*, Vol. 27, No. 5, 2002, pp. 290–299.

Elements of Spacecraft Design

Charles D. Brown, *Wren Software, Inc.*

This new book is drawn from the author's years of experience in spacecraft design culminating in his leadership of the Magellan Venus orbiter spacecraft design from concept through launch. The book also benefits from his years of teaching spacecraft design at University of Colorado at Boulder and as a popular home study short course.

The book presents a broad view of the complete spacecraft. The objective is to explain the thought and analysis that go into the creation of a spacecraft with a simplicity and with enough worked examples so that the reader can be self taught if necessary. After studying the book, readers should be able to design a spacecraft, to the phase A level, by themselves.

Everyone who works in or around the spacecraft industry should know this much about the entire machine.

Table of Contents:

❖ Introduction
❖ System Engineering
❖ Orbital Mechanics
❖ Propulsion
❖ Attitude Control
❖ Power System
❖ Thermal Control
❖ Command And Data System
❖ Telecommunication
❖ Structures
❖ Appendix A: Acronyms and Abbreviations
❖ Appendix B: Reference Data
❖ Index

AIAA Education Series
2002, 610 pages, Hardback • ISBN: 1-56347-524-3 • List Price: $111.95 • **AIAA Member Price: $74.95**

American Institute of Aeronautics and Astronautics
Publications Customer Service, P.O. Box 960, Herndon, VA 20172-0960
Fax: 703/661-1501 • Phone: 800/682-2422 • E-mail: warehouse@aiaa.org
Order 24 hours a day at www.aiaa.org

AIAA
American Institute of Aeronautics and Astronautics 02-0547